

Symmetry-breaking-dependent electronic structures and strain regulation in ReSeS monolayer

Texture Lin, J.W. Ma, H.C. Deng, L.Z. Liu

(School of Physics, Nanjing University, Nanjing 210033, China)

Abstract: Electronic devices for information storages and processes can be further optimized by introducing the degree of freedom of anisotropy, which is strongly dependent of their structural symmetry. Herein, a ReSeS monolayer with asymmetrical double-faces are proposed to disclose the anisotropic electronic structure. Meanwhile infrared fingerprint based on the lattice vibration is also adopted to demonstrate the symmetry-breaking-dependent structural transformation. First-principles calculations demonstrate that the geometry deformation will induce the reconstruction of electronic structure. Ulteriorly, both the dynamic properties of carrier and spectroscopic response can be regulated by external strain and displays anisotropic behaviors. Our idea provides threads for designing new regulable optoelectronic devices.

Key word: Anisotropy, ReSeS monolayer, Symmetry, Strain regulation

1. Introduction

The severe short-channel effect has limited the scaling down miniaturization of some semiconductor FETs such as metal-oxide-semiconductor [1]. It can be solved by thinning the crystal to the atomic level as two-dimensional (2D) material, in which the charge carriers will be more sensitive to scattering centers at dielectric channel interfaces when applying strain or doping impurity [2, 3]. One of the potential candidates is the family of the transition metal dichalcogenides (TMDs) due to their rich physical properties along with stable chemical properties [4-10]. Recently, MX_2 (M denotes a transition metal, X denotes a chalcogen) has received much attention due to its tremendous potential for applications [11-14]. Researchers in Jinran Yu's group demonstrated a mechano-photonic artificial synapse with synergistic multimodal synaptic plasticity by using graphene/MoS₂ heterostructure [15]. M. Baranowski's group reported a long-lived interlayer exciton emission in a MoS₂/MoSe₂/MoS₂ van der Waals heterostructure [16]. Chemical vapor deposition (CVD) was adopted to realize controllable syntheses of anisotropic ReX₂ monolayer, and the growth mechanism of low-lattice symmetric 2D materials was also clarified in these studies [17, 18]. Daniel A. Chenet's group argued the determination of the layer thickness could be realized through the strong anisotropy in the Raman scattering of few-layer ReS₂ [19]. All these works [15-24] indicate low symmetric electronic structure in TMD monolayer typically induces materials to exhibit anisotropic behaviors and bestows great application potential in nanoelectronics technology, such as novel electronic transport devices and optical devices.

However, works mentioned above have not reached the minimum of symmetry in TMD monolayers. Therefore, we further reduce the symmetry of ReX₂ monolayer through electronic reconstruction induced by symmetry breaking and suggests a new material "ReSeS". Based on the analysis about symmetry, the ReSeS monolayer can display a more excellent anisotropic characteristic. Infrared spectrum is adopted as a fingerprint to elaborate on the decrease in geometric symmetry. Due to the lower atomic symmetry configuration, the normal vibration modes will excite more infrared active and Raman active modes when coupling with the external electromagnetic field. Then the strain is applied to modulate the electronic structure and stress its anisotropy. Electronic reconstruction induced by the change of crystal spatial configuration has striking impacts on the electronic structure of ReSeS monolayer, and the influences will be further reflected in the electrical and spectral properties. The utilized strain will transform the band structure from near-direct feature to indirect feature. Different bending degrees at the G (Γ) point on the bottom of the conduction band (CBM) in first Brillouin zone (1-BZ) [25] result in anisotropy of the effective mass of electron. Meanwhile, anisotropic behaviors induced by the uniaxial strain along distinct directions can also be observed in both absorption and reflection spectra. This demonstrates the low symmetric electronic distribution again and produces a practical method for projecting minor geometry deformation.

2. Methods

The theoretical assessments were based on the density functional theory (DFT) with the Perdew-Burke-Ernzerh of generalized approximation (PBE, GGA), using CASTEP package code. A vacuum space of 25 Å was included into our

models to prevent the interaction between periodic layers. The plane-wave energy cut-off (E-cut) was set as 720.0 eV to expand the Kohn-Sham wave functions and the relaxations were carried out until below the convergence tolerances of energy as $1.0 \times 10^{-5.5}$ eV. The FFT grid in primitive cell is $45 \times 45 \times 192$. Monkhorst-Pack k-point meshes in 1-BZ were set as $4 \times 4 \times 1$, which have been tested for convergence.

3. Results and discussion

The structure of ReX_2 ($X=\text{S}, \text{Se}$) monolayer contains three atomic layers, in which the Re atoms are located in the middle layer and X atoms are located at double-face layers. The ReSeS monolayer is obtained by reconstructing the top and bottom layers in ReX_2 monolayer into S-layer and Se-layer, respectively. The structures of ReSe_2 , ReSeS , and ReS_2 monolayer are shown in Fig. 1(a)-1(c). There are only two types of Re and four types of X in the primitive cell of ReX_2 monolayer. As a comparison, ReSeS monolayer has more nonequivalent atoms due to the lower symmetry. There are four types of Re, four types of S, and four types of Se in the primitive cell of ReSeS monolayer. These three structures all belong to the 2D oblique system, and their lattice constants are listed in Table 1. OA and OB correspond to the OA and OB directions in Fig. 1(d). Considering these three structures have the same kind of Bravais lattice, we also display the Wigner-Seitz cell in their reciprocal spaces, namely 1-BZ, as Fig. 1(d). The directions reaching to the 6 high symmetry points in 1-BZ (G-A, G-C, G-B, G-D, G-F, G-M) from the central point G (Γ) are not equivalent, which is different from 2D materials with higher symmetry like MoS_2 monolayer and leads to more anisotropic feature in band structures.

To represent the anisotropy with more detail, we measured the bond lengths and populations of these three structures as Fig. 1(e)-1(g). Their distributions also exhibit pronounced anisotropy. The variance of the bond lengths S_l and populations S_p are calculated by using equation (1). Results are still shown in Table 1. The subscript x represents the l (bond lengths) or p (bond populations), the x_i is the value of i th bond lengths or populations and the \bar{x} is the average value. Se atoms have longer atomic radius and possess larger amount of charge. Therefore, the electronic distribution between Se and Re atoms will be denser, thus producing an increase in both bond populations and S_p . Meanwhile, the Re-Se bond lengths will also be longer and results in the expansion of lattice, which can be confirmed by comparing the lattice constants of these three structures. Moreover, due to the double-face structure, wave functions inside Re-S-layer and Re-Se-layer on longer satisfy the center-reversal symmetry. Therefore, the difference in polarity between Re-S bonds and Re-Se bonds makes the bond lengths in ReSeS monolayer have a more discrete distribution and leads to the largest S_l .

$$S_x = \frac{1}{24} \sum_{i=1}^{24} (x_i - \bar{x})^2 \quad (1)$$

Table 1

The lattice constants and the variance of bond lengths and populations of these 3 structures

	ReSe_2	ReSeS	ReS_2
OA (\AA)	6.739858	6.622116	6.502539
OB (\AA)	6.625071	6.514289	6.399352
$S_l (\times 10^{-3})$	3.74	5.56	3.31
$S_p (\times 10^{-3})$	6.21	4.67	2.34

Then we calculate the band structures and electrostatic potentials of these three structures as Fig. 2(a)-2(b) to further investigate the energy distribution of electronic structure. For the band structures without external strain, all of them exhibit a near-direct bandgap, i.e., the minimum of CBM is located at the G (Γ) point, and the maximum of the top of the valence band (VBM) is slightly offset from the G (Γ) point [in the range marked as red rectangles in Fig. 2(a)]. Similar phenomena are also found in other study [6], which can illustrate the accuracy of our measurements. Since both Se and S belong to the group 5A, and they are located in the fourth period and third period in periodic table of elements, respectively. The electronegativity of Se is smaller than that of S, and it signify a weaker attraction between Se atoms and electrons. Electrons distributed near Fermi level can be approximated as free electrons through pseudopotential method. Under a certain

pseudopotential, weaker attraction means the perturbation term of periodic potential field will produce a minor matrix element when acting with Bloch wave, thus generating a narrower bandgap. This is consistent with our measurements in Fig. 2(a) where their bandgaps are 1.358 eV for ReSe₂, 1.391 eV for ReSeS, and 1.467 eV for ReS₂. The greater electronegativity of S also creates stronger covalent-like interaction with Re, thus reducing the distance of polar-covalent Re-S bond. This also induces the spatial compression of electron clouds between S-layer and Re-layer and resulting in a potential difference of 1.5 eV as shown in Fig. 2(b). Meanwhile, the stronger coulomb attraction of S to electrons leads to a larger work function Φ_s , eventuating in discrepancy of work function with the Se-layer as $\Phi_s - \Phi_{se} = 0.409$ eV. These demonstrate that the double-face structure will prompt the electrostatic potential to have an anisotropic distribution. Besides, the energy distribution of electronic structure in ReSeS monolayer can be intuitively reflected through the density of states (DOS) as Fig. 2(d). The s orbitals are predominant in the region (-14 eV ~ -11 eV) far from the Fermi level, while in the region (-7 eV ~ 5 eV) near the Fermi level the d and p orbitals play a major role. Because the ReSeS is a covalent-like crystal and the valence-electron-configurations of Re, Se, and S atoms are $5d^5 6s^2$, $4s^2 4p^4$, and $3s^2 3p^4$ respectively, the energy of VBM highly depends on the Re-d and Se-p electrons.

However, neither the bond properties (like length or population) nor the energy distribution of electronic structure can effectively highlight the geometric symmetry of ReSeS monolayer to the greatest extent, resulting in the insufficient understanding of the anisotropy. Therefore, we use infrared spectrum, a powerful tool, as fingerprint to reflect the macroscopic symmetry. For the ReX₂ (X = S, Se) monolayer. Its primitive cell satisfies both the immobility operation and the central inversion operation. This indicates that ReX₂ monolayer is isomorphic to the point group C_i [27, 28]. The symmetry breaking induced by the double-face structure in ReSeS monolayer leads to the central inversion operation on longer be satisfied. So, the ReSeS monolayer is isomorphic to the simplest point group C_1 . Centrosymmetric vibrations of atoms in ReX₂ will cause the transformations of the polarization. These vibration modes will induce Stokes or Anti-Stokes scattering of the incident photon and results in becoming Raman active modes. However, such vibrations do not significantly alter the dipole moments between atoms, so they do not have infrared activity. Relatively, the infrared active modes in ReX₂ do not change the polarization as well and exhibit no Raman activity. However, double-face structure in ReSeS produces the polar moments between Se-layer and S-layer. Thus, the polarization and dipole moments can be transformed concurrently, and more vibration modes have both infrared and Raman activity will be generated. The infrared spectra of these three structures are displayed in Fig. 2(a). ReSeS has 36 infrared active modes while ReSe₂ and ReS₂ just possess 15 active modes. Both ReX₂ and ReSeS have 12 atoms in primitive cell, and each atom contains 3 degrees of freedom. According to the harmonic oscillator approximation, the potential energy V of crystal can be expressed as equation (2), where the r_{ijk} represents the displacement of the j th atom along the k direction in the i th cell [$i = (i_1 \ i_2)$] and R_i represents the coordinates of the i th cell. Then we can obtain the dispersion relation $\omega(\mathbf{q}_0)$ through equation (3), where \mathbf{q}_0 is the lattice wave vector at G (Γ) point and m_j is the mass of j th atom. A wave vector \mathbf{q}_0 will correspond to 36 vibrational frequency branches, and in turn to form 36 normal vibration modes. By distinguishing the motion of the center of mass from the relative motion among atoms, we can divide the 36 branches into 3 acoustic branches and 33 optical branches. The 36 modes in the ReX₂ monolayer can be expressed by irreducible representation as $C_i = 18A_g \oplus 18A_u$, 15 A_u modes ($4A_u \sim 18A_u$) are infrared active modes and 18 A_g modes are Raman active mode. The vibration modes of ReSe₂ and ReS₂ are listed in Table S1 and S2, respectively. As mentioned above, there are no mode in ReX₂ possess infrared and Raman activity simultaneously. The ReSeS monolayer also has the irreducible representation as $C_1 = 36A$, and 33 optical branches (A4 ~ A36) have both infrared activity and Raman activity. The frequencies and their corresponding modes are listed in Table 2.

Table 2

Raman shifts of 33 Raman peaks in the ReSeS monolayer			
modes	Raman shift	modes	Raman shift
	(cm^{-1})		(cm^{-1})

A4	114.41	A21	246.09
A5	122.79	A22	256.08
A6	126.08	A23	264.01
A7	128.03	A24	268.85
A8	134.47	A25	277.70
A9	144.21	A26	281.12
A10	165.47	A27	293.85
A11	175.82	A28	297.09
A12	182.30	A29	302.98
A13	191.72	A30	305.35
A14	201.57	A31	323.63
A15	205.02	A32	343.47
A16	209.36	A33	356.70
A17	212.72	A34	382.28
A18	224.88	A35	403.62
A19	227.50	A36	427.55
A20	234.20		

$$V = \frac{1}{2} \sum_{\ddot{u}\ddot{v}\ddot{w}\ddot{x}} \left(\frac{\partial^2 V}{\partial \mathbf{r}_{ijk} \partial \mathbf{r}_{i'j'k'}} \right) \mathbf{r}_{ijk} \mathbf{r}_{i'j'k'} = \frac{1}{2} \sum_{\ddot{u}\ddot{v}\ddot{w}\ddot{x}} \Lambda_{jkj'k'} (\mathbf{R}_i - \mathbf{R}_{i'}) \mathbf{r}_{ijk} \mathbf{r}_{i'j'k'} \quad (2)$$

$$\Gamma_{jkj'k'}(\mathbf{q}_0) = \sum_{i-i'} \Lambda_{jkj'k'} (\mathbf{R}_i - \mathbf{R}_{i'}) e^{-iq_0 \cdot (\mathbf{R}_i - \mathbf{R}_{i'})}$$

$$\left| \Gamma_{jkj'k'}(\mathbf{q}_0) - \omega^2 m_j \delta_{jk}^{j'k'} \right|_{3n \times 3n} = 0 \quad (n = 12) \quad (3)$$

We mainly focus on the 4 typical Raman peaks (A8, A28, A31, A34) in the Raman spectroscopy and analyze the vibrations of the atoms in these modes. The mode with large out-plane vibrational weights, large in-plane vibrational weights and both salient in-plane and out-plane vibrational weights can be denoted as A_g -like, E_g -like and C_p -like mode respectively [29]. The polarized internal field induced by the lattice vibration is strongly coupled with the infrared electromagnetic field, and the responses of atoms to the external field are influenced by their relative atomic mass. As Fig. 3(b), since the degeneracy of orthonormal modes is removed, vibrations of Re and Se with larger mass are asymmetric to the Re-layer when being coupled with low-frequency field, thus making A8 as C_p -like mode. Similarly, the low symmetric vibrations dominated by Se and S in the middle-frequency region causing A28 to become C_p -like mode as well. However, in the high-frequency region, only S having smaller mass has a prominent vibration when responding to the external field, so it is easy to distinguish A31 and A34 as E_g -like and A_g -like modes respectively. In addition, in order to identify the different vibrational modes, we also calculated the Raman intensity with parallel configuration $I(\theta)$ using equation (2) (see P2 in supporting information). \mathbf{R} is the Raman tensor which can be expressed as a 3×3 symmetric matrix, \mathbf{v}_i is the direction of the electric field of incident light (linear-polarized) and θ is the angle between electric field and X-axis. We called Y-axis as zigzag direction due to the spatial composition of Re atoms shown in Fig. 1(b) (thick red line) along this direction. The anisotropic Raman intensities of the above 4 Raman modes are also exhibited in Fig. 3(b), and the rest are displayed in Fig. S1. We observe that along the zigzag, only the A28 mode produces stronger intensities, while both the A31 mode and A34 mode produce stronger Raman intensities along the direction perpendicular to the zigzag. Therefore, the modes can be distinguished by applying polarization measurement, and the ReSeS monolayer can be identified by the orthonormal vibrational modes which reflects information of macroscopic symmetry through crystallographic point group to effective advantage.

Considering electronic reconstruction induced by symmetry breaking in ReSeS monolayer produces more abundant anisotropic behaviors compared to the conventional ReX_2 . Geometry deformation is also a practical method to regulate the electronic structure and heighten the anisotropy of the material [30, 31]. Therefore, as Fig. 2(c), the transformations of band

structure of ReSeS monolayer with applying strain along OA and OB directions as well as biaxial strain are investigated. The strain scaling factor in OA and OB directions are defined as $\alpha_A = (A - A_0) / A_0$ and $\alpha_B = (B - B_0) / B_0$, where A and B are the lengths of lattice in the OA and OB directions after deformation, and A_0 and B_0 are the lattice constants in OA and OB directions. We find that in the region of -2% ~ 4% strain, the bandgaps will narrow with the degree of deformation increase, but their band features remain as the near-direct. However, when the strain is applied to -4% along OA direction, 6% along OB direction, and -4% with the biaxial deformation, significant drops will occur in the CBM near the high symmetry point around the G (Γ) point, and thus forming the indirect bandgap. The differences between near-direct and indirect bandgap under these situations are 0.075 eV for OA strain, 0.154 eV for OB strain, and 0.206 eV for biaxial strain, respectively. It illustrates that applying strain will definitely transform the band structure. Moreover, these changes further produce the variation in electrical and spectral properties [32].

Immediately afterward we examine the change in electrical, and spectral properties with strain applied separately. For electronic properties, the effective mass of electron has significant impacts on electrical transport properties and short-wavelength optical device design [33]. As semiconductors like ReSeS, whose physical properties depend mainly on the band structure at the band edges, the $\mathbf{k} \cdot \mathbf{p}$ method is a common approach to calculate the band structure near the high symmetry point. We choose the strain range (OA strain: -2% ~ 6%, OB strain: -4% ~ 4%) that keeps the band feature as near-direct to compare the effective mass of electrons at G point along different directions in 1-BZ, and the effective mass of electrons along i direction can be defined as m_i by equation (3). m_e is the mass of electron, \mathbf{k}_i is the Bloch wave vector along i direction and $\mathbf{k}_0 = 0$ represents the wave vector at the G point. $E_n(\mathbf{k})$ is the energy of n th energy band and $u_n(\mathbf{k})$ is the periodic factor of Bloch wave at this band. The energy of the CBM is defined as $E_C(\mathbf{k})$. As the red arrow in Fig. 4, with the increase of α_A , the overlap of wave functions of conduct band will be tighter, leading to the overlap integral increases and band width widens, thus growing the bending degree at the G (Γ) point in the CBM and reducing the m_i . The m_i will change contrarily with the raise of α_B for the similarly reasons. Then as the black arrow in Fig. 3, the m_i bespeaks obvious anisotropy under the regulation of strain. the increase of α_A will shift the maximum of m_i from the direction G-B to G-F, while the increase of α_B will cause a significant change in the m_i in direction G-C. The electronic transport properties are closely related to the carrier mobility μ , which can be calculated by thermodynamics and expressed as $e\bar{\tau}_i / m_i$. e is the elementary charge, m_i is the effect mass of electron in i direction, and the $\bar{\tau}_i$ means the relaxation time in i direction. The electrons will exhibit more localized behaviors with large m_i and resulting in smaller mobility. Conversely, electrons with smaller m_i tend to have non-local probability density distribution in the periodic potential field, and make the material produce better electronic transport properties. These relationships demonstrate important influence of m_i in the electrical conductivity, which in turn reflects the potential of strain engineering for applications in modulating electrical properties of ReSeS monolayer.

$$\frac{1}{m_i} = \frac{1!}{m_e} + \frac{2!}{m_e^2} \sum_{n \neq C} \frac{|\langle u_C(\mathbf{k}_0 = 0) | -i\hbar \nabla_i | u_n(\mathbf{k}_0 = 0) \rangle|^2}{E_C(\mathbf{k}_0 = 0) - E_n(\mathbf{k}_0 = 0)} = \left[\frac{1}{\hbar^2} \left(\frac{\partial^2 E_C(\mathbf{k})}{\partial |\mathbf{k}_i|^2} \right)_{\mathbf{k}=\mathbf{k}_0=0} \right] \quad (4)$$

For the spectral properties, the direction of incident light is along the Z-axis. Dielectric function ε ($\varepsilon = \varepsilon_1 + i\varepsilon_2$) determines the various optical properties of the material. It consists of real part ε_1 and imaginary part ε_2 , and their relationship can be roughly given via the K - K relationship as equation (4). Then the absorption and reflection spectra of ReSeS monolayer are examined through the equation (5) and equation (6) respectively. C is principal part of integral and E is the energy of photon. I means absorption intensity and R means reflectivity. Reflection spectrum, absorption spectrum along with dielectric function without geometry deformation are calculated as Fig. 5(a)-5(b). We find that both absorption and reflection spectrum have two peaks. The reflection peak 1 is in the visible region, and other 3 peaks are all in the ultraviolet region. Dielectric materials have different response mechanisms to electromagnetic waves in different frequency regions. The rotation of molecules' multipole moment caused by external electromagnetic fields dominates in the microwave region, and the electromagnetic wave with high frequency in the infrared region will be coupled with the polarization of ions strongly. Next, as the frequency further increases, the electromagnetic wave at visible along with

ultraviolet region will cause the separation between the electron and nuclei. Compared to the infrared region, this will produce more significant consumption and embodies in the protrusions of ε_2 within 5 eV ~ 12 eV as Fig. 5(b). According to the shift of the spectral peaks and the relative intensity of peaks defined as peak 1 divided by peak 2 shown in Fig. 5(c)-5(f), the application of strain leads to the anisotropy behaviors exhibited by the spectra. Within the range where band structure possesses near-direct bandgap, absorption peak 1 and peak 2 undergo redshift and blueshift respectively with the increase in α_A , while exhibiting the opposite trends when α_B is increased. The energy conservation relationship of electronic transition is $E_n(\mathbf{k}) - E_n(\mathbf{k}) = E$, where $E_n(\mathbf{k})$ is the energy of n th energy level, \mathbf{k} is the wave vector, E is the energy of incident photon. Because the increase of α_A leads to proximity of two absorption peaks. Incident photons with definite energy could excited more electrons to transition to higher energy level, thereby reducing the relative intensity of absorption peaks. Similarly, the separation of peaks caused by the increase of α_B have the contrary effect. These are consistent with our results in Fig. 5(c)-5(d). The strain applied along OA direction will cause variation of bandgap more significant as Fig. 2(c), reflecting the larger change range of energy level splitting and resulting in more prominent redshift in reflection peaks. Taking the visible light peak (reflection peak 1) as an example, the OA strain turns the wavelength from 454 nm to 644 nm, while the wavelength only changes from 464 nm to 619 nm with OB strain. The redshift of the visible light peak is more pronounced, which indicates that the difference of two reflection peaks will go up with the increase of either α_A or α_B . It also causes the relative-blueshift of the higher energy level and induces that fewer electrons can leap to this level by absorbing definite energy. Ultimately, the relative intensity of reflection peaks will increase overall as Fig. 5(e)-5(f). The discrepancies in both absorption and reflection spectra provide an effective method to distinguish strain exerted. The strain-dependended spectrum can also be used to design simple optical-mechanical adjustment devices. What's more, the reflection peak 1 in visible region makes this material have potential for some optical instruments combined with human eyes.

$$\varepsilon_2 = \frac{2E}{\pi} C \int_0^{\infty} \frac{\varepsilon_1}{E - \zeta} d\zeta \quad (4)$$

$$I = \frac{E}{\hbar} \left[2(|\varepsilon| - \varepsilon_1) \right]^{\frac{1}{2}} \quad (5)$$

$$R = \left| \frac{\sqrt{\varepsilon} - 1}{\sqrt{\varepsilon} + 1} \right|^2 \quad (6)$$

4. Conclusion

In summary, the first-principles calculations are used to compare electronic structure of ReS₂, ReSeS, and ReSe₂ monolayer, and the anisotropy induced by symmetry breaking of ReSeS is highlighted firstly. Because of the symmetry breaking, the orthonormal vibration modes of the lattice will relieve the degeneracy, and further stimulate more Raman-active modes when they are coupling with external field. Therefore, Raman spectroscopy can be used as a fingerprint to identify ReSeS monolayer while parallel configuration is used to distinguish various orthonormal modes and present their anisotropy. Then the variations in its electrical and spectral properties which are induced by the electronic reconstruction caused by the geometry deformation are investigated. The results indicate the electronic transport properties based on anisotropic effective mass of electron can be modulated by external strain. Meanwhile, anisotropic behaviors in reflection and absorption spectra are mainly reflected in redshift and blueshift of absorption and reflection peaks along with the transformations of their relative intensity. It will produce an effective method to observe macroscopic deformation of the lattice for achieving strain regulation. Furthermore, we figure out the atomic defects can enhance the conductivity by inducing defect levels and the S1-V along with S3-V are easier to generate. The thermodynamic conclusions guarantee the stability of formation and migration of vacancies. The EOv of S3-V will mutate under specific strain due to a more stable bonding between Re4 and S1 arguing the density of vacancy can be regulated by external strain. Considering the external strain can be realized by adding specific substrates in laboratory-made or industrial manufacturing, these results above

indicate the ReSeS monolayer has enormous application potential.

5. Acknowledgement

Our work is greatly supported by the School of Physics of Nanjing University, and we also thank for the computational resources provided by High Performance Computing Center of Shenzhen.

6. References

- [1] Liu, E., Fu, Y., Wang, Y. et al. Integrated digital inverters based on two-dimensional anisotropic ReS₂ field-effect transistors. *Nat Commun* 6, 6991 (2015).
- [2] Zhang, C., Tu, T., Wang, J. et al. Single-crystalline van der Waals layered dielectric with high dielectric constant. *Nat. Mater.* (2023).
- [3] Qiao, J., Kong, X., Hu, Z.X. et al. High-mobility transport anisotropy and linear dichroism in few-layer black phosphorus. *Nat Commun* 5, 4475 (2014).
- [4] Peymon Zereszki, Peng Yao, Dawei He, Yongsheng Wang, and Hui Zhao, *Phys. Rev. B* 99, 195438 (2019).
- [5] Liu, E., Long, M., Zeng, J., Luo, W., Wang, Y., Pan, Y., Zhou, W., Wang, B., Hu, W., Ni, Z., You, Y., Zhang, X., Qin, S., Shi, Y., Watanabe, K., Taniguchi, T., Yuan, H., Hwang, H.Y., Cui, Y., Miao, F. and Xing, D. (2016), *Adv. Funct. Mater.* 26: 1938-1944.
- [6] Tongay, S., Sahin, H., Ko, C. et al. Monolayer behaviour in bulk ReS₂ due to electronic and vibrational decoupling. *Nat Commun* 5, 3252 (2014).
- [7] Ashish Arora, Jonathan Noky, Matthias Drüppel, Bhakti Jariwala et al. *Nano Letters* 2017 17 (5), 3202-3207.
- [8] Chris M. Corbet, Connor McClellan, Amritesh Rai, Sushant Sudam Sonde, Emanuel Tutuc, and Sanjay K. Banerjee. *ACS Nano* 2015 9 (1), 363-370.
- [9] Chhowalla, M., Shin, H., Eda, G. et al. The chemistry of two-dimensional layered transition metal dichalcogenide nanosheets. *Nature Chem* 5, 263–275 (2013).
- [10] Wang, Q., Kalantar-Zadeh, K., Kis, A. et al. Electronics and optoelectronics of two-dimensional transition metal dichalcogenides. *Nature Nanotech* 7, 699–712 (2012).
- [11] Hai Li, Jumiati Wu, Zongyou Yin, and Hua Zhang *Accounts of Chemical Research* 2014 47 (4), 1067-1075.
- [12] X. Zhang, Z. Lai, C. Tan, H. Zhang, *Angew. Chem. Int. Ed.* 2016, 55, 8816.
- [13] Shi, J., Ji, Q., Liu, Z., Zhang, Y. (2016). *Adv. Energy Mater.* 6: 1600459.
- [14] M. Baranowski, A. Surrente, L. Klopotoski, J. M. Urban, N. Zhang, D. K. Maude, K. Wiwatowski, S. Mackowski, Y. C. Kung, D. Dumcenco, A. Kis, and P. Plochocka. *Nano Letters* 2017 17 (10), 6360-6365.
- [15] Jinran Yu, Xixi Yang, Guoyun Gao, Yao Xiong et al. *Science Advances*, Volume 7, 12 (2012).
- [16] Cui, Fangfang et al. "Epitaxial growth of large-area and highly crystalline anisotropic ReSe₂ atomic layer." *Nano Research* 10, 8 (August 2017): 2732-2742.
- [17] Quan, W., Pan, S., Zhou, F. et al. Anisotropic monolayer of ReX₂ on Au foils for exploring abnormal growth behavior and electronic properties. *Nano Res.* 16, 4197–4210 (2023).
- [18] Bhakti Jariwala, Damien Voiry, Apoorv Jindal, Bhagyashree A. Chalke, Rudheer Bapat, Arumugam Thamizhavel, Manish Chhowalla, Mandar Deshmukh, and Arnab Bhattacharya. *Chemistry of Materials* 2016 28 (10), 3352-3359.
- [19] Daniel A. Chenet, Burak Aslan, Pinshane Y. Huang, Chris Fan, Arend M. van der Zande, Tony F. Heinz, and James C. Hone. *Nano Letters* 2015 15 (9), 5667-5672.
- [20] Yung-Chang Lin, Hannu-Pekka Komsa, Chao-Hui Yeh, Torbjörn Björkman, Zheng-Yong Liang, Ching-Hwa Ho, Ying-Sheng Huang, Po-Wen Chiu, Arkady V. Krasheninnikov, and Kazu Suenaga. *ACS Nano* 2015 9 (11), 11249-11257.
- [21] Deniz Çakır, François M. Peeters, and Cem Sevik, "Mechanical and thermal properties of h-MX₂ (M = Cr, Mo, W; X = O, S, Se, Te) monolayers: A comparative study", *Appl. Phys. Lett.* 104, 203110 (2014).
- [22] Z.H. Zhou, B.C. Wei, C.Y. He, Y.M. Min, C.H. Chen, L.Z. Liu, X.L. Wu, *Applied Surface Science*, Volume 404, 2017, 276-281.
- [23] Enze Zhang, Peng Wang, Zhe Li, Haifeng Wang et al. *ACS Nano* 2016 10 (8), 8067-8077.
- [24] Sim, S., Lee, D., Trifonov, A.V. et al. Ultrafast quantum beats of anisotropic excitons in atomically thin ReS₂. *Nat*

Commun 9, 351 (2018).

[25] Shengxue Yang, Cong Wang, Hasan Sahin, Hui Chen, Yan Li, Shu-Shen Li, Aslihan Suslu, Francois M. Peeters, Qian Liu, Jingbo Li, and Sefaattin Tongay. *Nano Letters* 2015 15 (3), 1660-1666.

[26] Vitor M. Pereira and A. H. Castro Neto. *Phys. Rev. Lett.* 103, 046801. 20 July 2009.

[27] Showkat Hassan Mir, Vivek Kumar Yadav, and Jayant Kumar Singh. *ACS Omega* 2020 5 (24), 14203-14211.

[28] Masakatsu Suzuki, Takeshi Uenoyama, and Akira Yanase. *Phys. Rev. B* 52, 8132. 15 September 1995.

[29] Amber McCreary, Jeffrey R. Simpson, Yuanxi Wang et al. *Nano Letters* 2017 17 (10), 5897-5907.

[30] Yanqing Feng, Wei Zhou, Yaojia Wang, Jian Zhou, Erfu Liu et al. *Phys. Rev. B* 92, 054110.

[31] Hamidreza Zobeiri, Nicholas Hunter, Ridong Wang, Xinman Liu, Hong Tan, Shen Xu and Xinwei Wang. *Nanoscale Adv* 2020, 2, 5821.

[32] Z. H. Zhou, Y. M. Min, X. X. Liu, J. Q. Ding, J. H. Guo, F. R. Hu, and L. Z. Liu, Regulation of oxygen vacancy types on SnO₂ (110) surface by external strain, *AIP Advances* 6, 055102 (2016).

[33] Rui Li, Yang Han, Ting Hu, Jinming Dong, and Y. Kawazoe. *Phys. Rev. B* 90, 045425. 28 July 2014.

FIGURES:

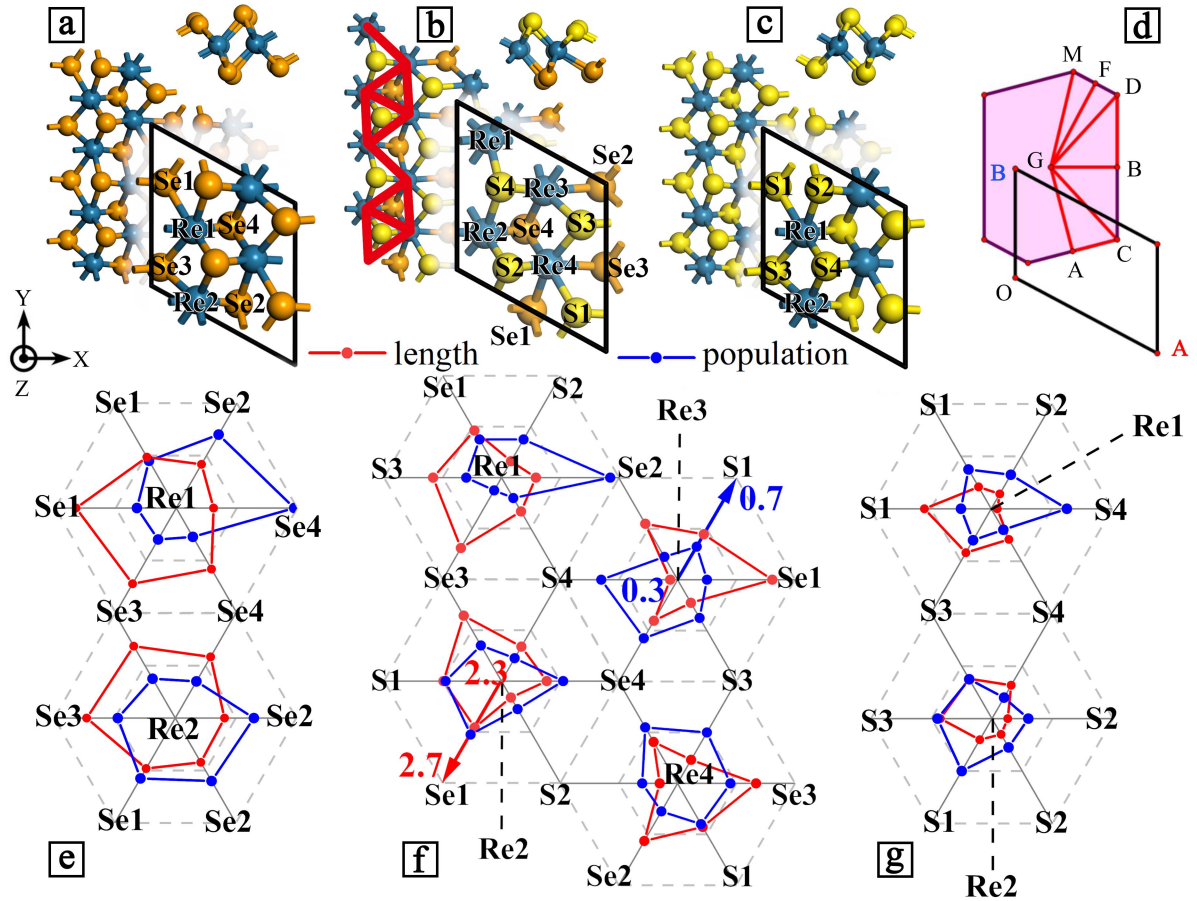


Fig. 1 (a)-(c) The structure and primitive cell of ReSe_2 , ReSeS , ReS_2 monolayer respectively. Thick red line in (b) mean zigzag direction. (d) The diagrammatic sketch of 1-BZ (purple region) and primitive cell (black line marked OA and OB) of two-dimensional oblique lattice system. (e)-(g) The bond lengths and populations of ReSe_2 , ReSeS , ReS_2 monolayer respectively.

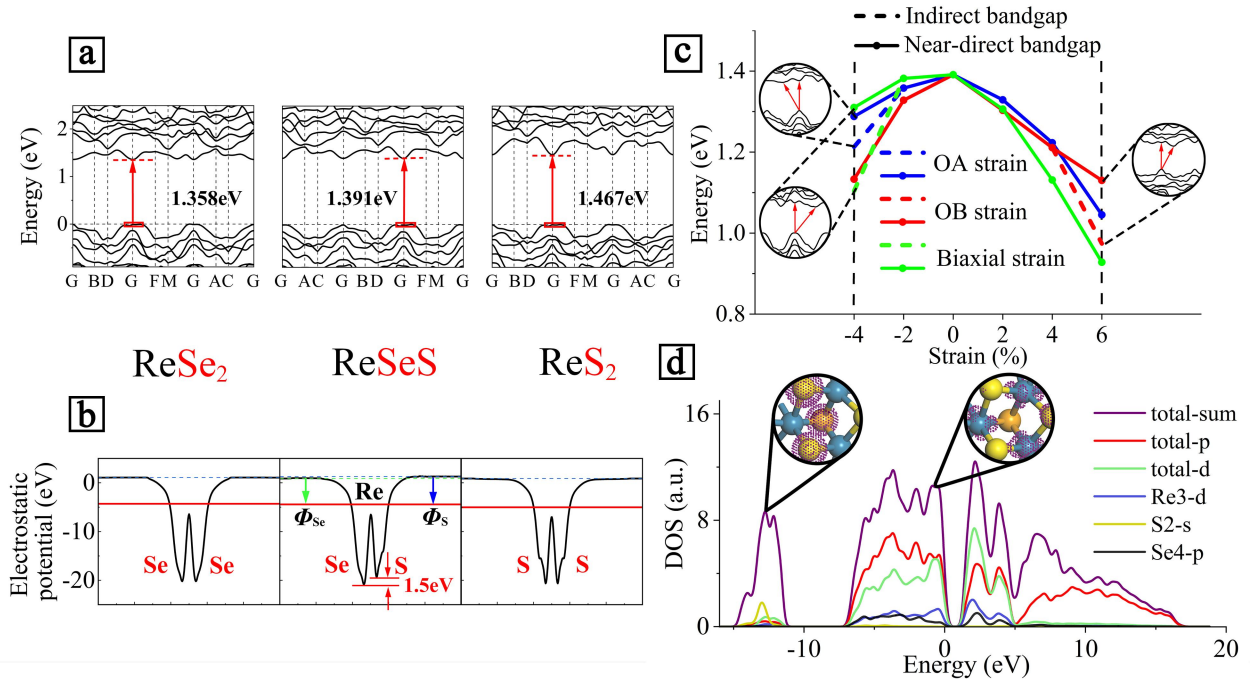


Fig. 2 (a) The band structure of ReSe_2 , ReSeS , ReS_2 monolayer without strain respectively. The tiny red rectangles at VBM represent the range of small undulations near the G (Γ) point which causes the near-direct bandgap. (b) The electrostatic potential of ReSe_2 , ReSeS , ReS_2 monolayer without strain respectively. The red line is Fermi level, dotted green line and dotted blue line is the bottom and

top vacuum level. Φ_s and Φ_{se} is the work functions corresponding to S-layer side and Se-layer side. (c) The bandgap of ReSeS monolayer with different strain. Solid line means near-direct bandgap. Dotted line means indirect bandgap. Figures in black circles present the indirect bandgap briefly. (d) The DOS of ReSeS monolayer without strain. Total means total atoms in primitive cell and sum means all kinds of orbitals

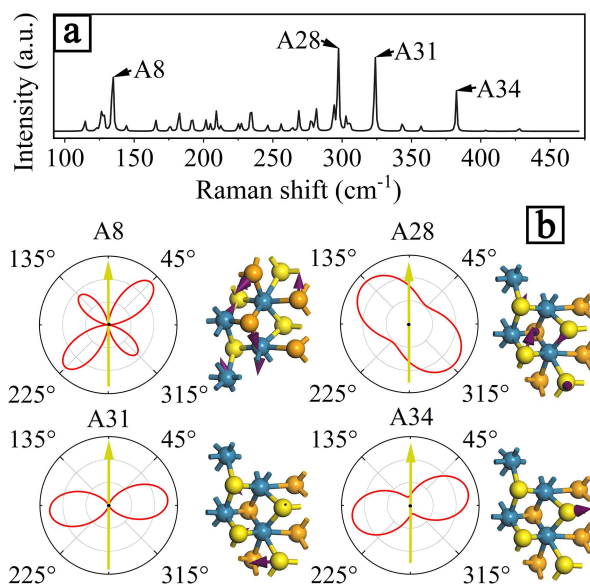


Fig. 3 (a) Raman spectrum of ReSeS monolayer. (b) The vibration and the Raman intensity with parallel configuration of 4 prominent Raman peaks. The yellow arrow is the direction of zigzag.

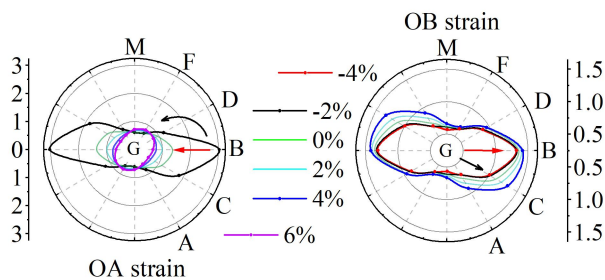


Fig. 4 The effective mass of electron (m_e^*) of ReSeS monolayer in all directions to the high symmetry points with strain along OA and OB directions.

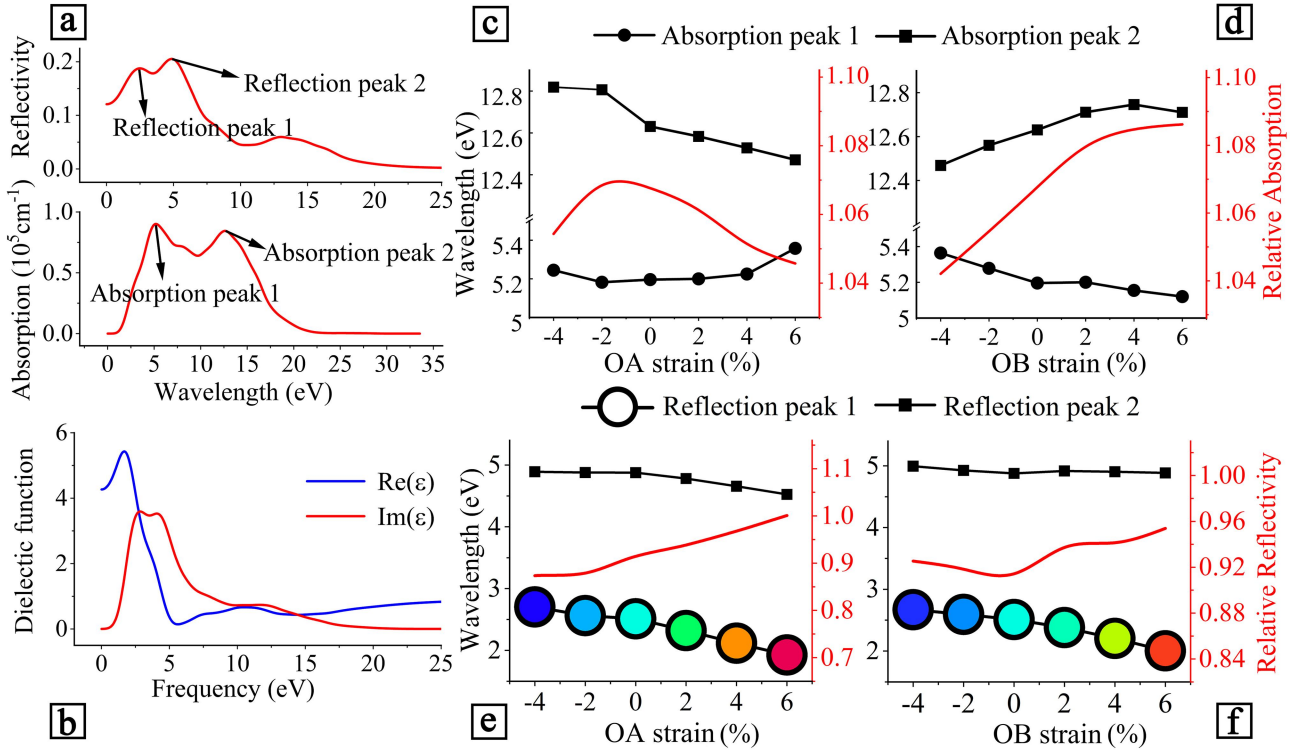


Fig. 5 (a) The reflection and absorption spectrum of ReSeS monolayer without strain. Both the two absorption peaks and two reflection peaks are marked in (a). (b) The dielectric function ϵ of ReSeS monolayer along with its real and imaginary parts. (c)-(d) The energy of absorption peaks and relative intensity of two peaks of ReSeS monolayer with strain along OA and OB directions. (e)-(f) The energy of reflection peaks and relative reflectivity of two peaks of ReSeS monolayer with strain along OA and OB directions. The colorful reflection peak 1 is the visible light peak and the colors correspond to their wavelengths.

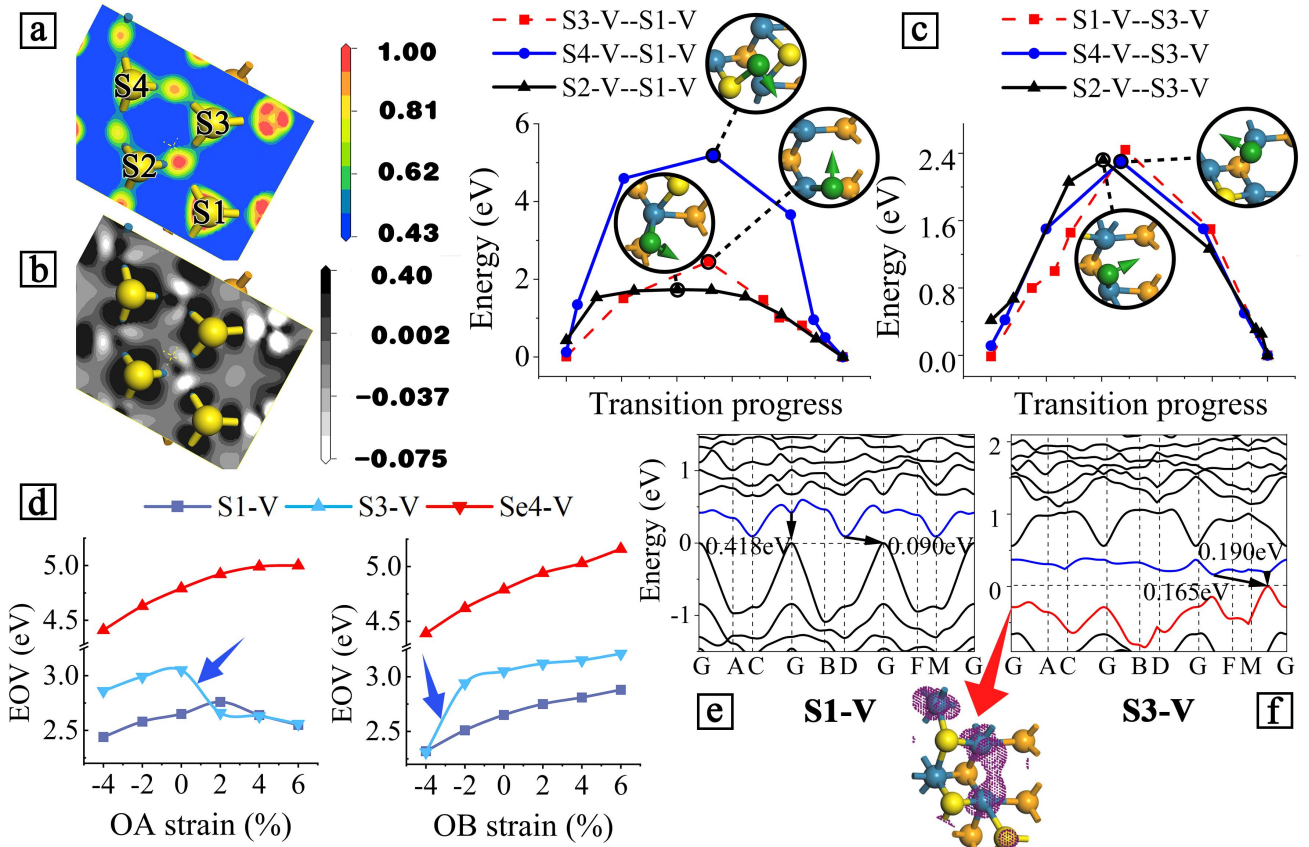


Fig. 6 (a) The electron density of all S-Re bonds. The color close to red corresponds to the greater electron density. (b) The electron density difference of all S-Re bonds. The black means losing charge and the white means gaining charge. (c) 5 kinds of vacancy migration processes. The migration between S3-V and S1-V are marked as red dotted line which is displayed both in 2 figures in (c). transition states in these processes are shown in black circles. The green atom in black circle is the migrating S atom and the green arrow is the vibration caused by virtual frequency generated by the transition state. (d) variations of EOv of S1-V, S3-V and Se4-V structures with strain applied along OA and OB directions. The energy mutation generated during the application of strain is marked by the blue arrow. (e) The band structure of S1-V structures. Defect level, i.e., donor level is marked as blue line. (f) The band structure of S3-V structures. Defect levels are marked with blue and red for donor and acceptor level respectively. Red arrow exhibits the orbitals correspond to the acceptor level.